

HETG Update

The HETGS Team

The HETGS at 20 (well, really 40)

This year we celebrate the 20th anniversary of the launch of the *Chandra* X-ray Observatory. In fact, the origins of the High Energy Transmission Grating Spectrometer (HETGS) go back 20 years earlier, to 1979. That was when Claude Canizares (HETG Instrument PI) and Mark Schattenburg initiated a collaboration with an MIT colleague in electrical engineering, Henry I. Smith, to develop the periodic nanostructures that would become the High Energy Grating (HEG) and Medium Energy Grating (MEG) elements (for details, see Canizares et al. 2005).

Our primary goal was to find a way to fabricate short period transmission grating facets (0.2 μm for HEG and 0.4 μm for MEG) that were thick enough ($\geq 0.5 \mu\text{m}$ gold) to give good efficiency up to the Fe K line near 7 keV (for the HEG), rugged enough to survive launch vibration and acoustic loads—but with a support membrane thin enough to transmit down to 0.5 keV, and large enough ($\approx 6 \text{ cm}^2$) so a reasonable number of facets (a few hundred) would cover the *Chandra* telescope aperture. Furthermore, the fabrication process had to be controlled well enough to produce those hundreds of grating facets with nearly identical periods (to within ≤ 100 ppm) so, when aligned to high enough tolerance on a suitable fixture, their spectra would overlap with little degradation. The final HETGS system, consisting of the High Resolution Mirror Assembly (HRMA), the HETG assembly and ACIS-S, would give high spectral resolution ($\lambda/\Delta\lambda$ of up to 1000) with reasonable effective area over the 0.5 to 7 keV band.

It took a good fraction of the next 20 years and the innovative talents of Mark and numerous other researchers to achieve those goals. By 1984 we had demonstrated a viable method for grating fabrication, and we were selected by NASA for Phase B development in 1985. At that time, AXAF (later renamed *Chandra*) was eight years from launch, and it remained eight years from launch for the next eight years. During that time we continued improving grating fabrication methods. There were also setbacks and even a near-death experience: in 1993 the supplier of a new, one-of-a-kind high intensity X-ray generator, which was essential to our intended fabrication process (and cost several million dollars), went bankrupt and was unable to deliver a working tool. This loss, just as we were about to start large-scale production, forced us to radically alter the method of grating fabrication. Miraculously, using the experience gained over the previous 14 years, Mark and colleagues rapidly devised an alternative production process that allowed us to meet our specified performance goals, within budget

and on schedule. In 1996 we delivered the fully assembled HETG for calibration, integration and testing.

High resolution X-ray spectroscopy, as enabled by the HETGS (also the Low Energy Transmission Grating [LETG] and XMM-Newton Reflection Grating Spectrometer [RGS]), gives observers a powerful tool for probing the physics of astronomical objects. To date, well over one thousand observations of some 400 targets have been performed with the HETGS, including nearly every category of X-ray emitting astronomical object. Spectroscopy of emission lines enables the determination of physical parameters such as plasma temperature, emission measure distribution vs. temperature, degree of ionization, elemental abundance, Doppler velocity, density, and degree of non-equilibrium. Absorption line spectroscopy can reveal the presence and physical conditions of winds and outflows, the content and even the molecular composition of circum-stellar and inter-stellar matter, and the presence of a hot Galactic halo. In the rest of this update, we present some illustrative examples of HETGS science from the past two decades.

The Hybrid Stellar Wind of θ^1 Ori C

The fact that some massive stars emit hard X-rays and some do not came a bit as a surprise to the stellar community in the early phases of the *Chandra* mission (*Chandra* press release, Nov. 9, 2000). The standard model is based on line-driven shock instabilities accelerating wind plasma to high velocities. This model predicts soft X-ray emissions up to about 20 MK in extreme cases, broad and asymmetric lines, and in some cases measurable blueshifts caused by self absorption in the wind. A prototype of such a wind was observed in the very early supergiant ζ Pup (Cassinelli et al. 2001). In contrast, Fig. 1 shows the X-ray spectrum of θ^1 Ori C in the Orion Trapezium. This spectrum is dominated by fairly narrow K- and L-shell emission lines from a broad range of plasma temperatures from 10 MK to 80 MK. This includes H-like and He-like lines from most abundant elements in the X-ray band between 0.4 and 7 keV (Schulz et al. 2003). Most impressive are K-lines from S xv, S xvi, Ar xvii, Ar xviii, and Ca xix, Ca xx as well as the forest of L-shell lines from Fe xvii to Fe xxiv (see insets in Fig. 1). The spectrum also shows that we are observing a hybrid wind in which most of the hard lines originate from a magnetically confined plasma, and the soft lines from an unconfined stellar wind (Schulz et al. 2003; Gagne et al. 2005). Resolving He-like triplet lines in massive stars provides a unique diagnostic tool as the flux ratio of the forbidden to intercombination line component is directly related to the UV flux (see below) and hence to the distance of the emitting ions from the stellar photosphere.

Plasma Density and UV Flux Diagnostics

The X-ray band covered by the HETG includes several radiative ionic transitions from meta-stable upper levels

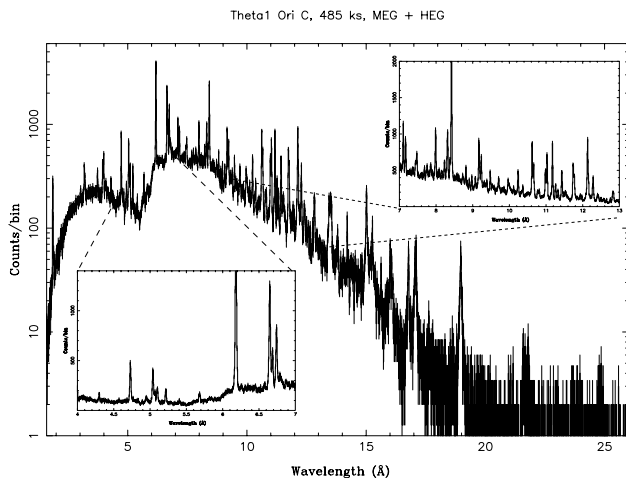


Figure 1: The HETGS Orion Legacy Project so far collected 485 ks exposure of the young O5.5V star θ^1 Ori C. The long exposure yields a high definition X-ray spectrum of a collisionally ionized plasma with temperature of up to 80 MK. The left inset shows the resolved S XV and Si XIII triplets at 5.06 Å and 6.68 Å. The right inset shows the Fe XXIX dominated line region of the hot plasma (see also Schulz et al. 2003).

of abundant elements. Of particular interest are the electric dipole forbidden (f) transitions of the He-like ions of O, Ne, Mg, and Si, which the HETGS can clearly resolve from the nearby resonance and intercombination lines (commonly referred to as r and i). The metastable f-line's upper level is long-lived enough to be de-populated by collisional excitation or by UV photo-excitation, if the electron or UV flux densities are great enough. Hence, ratios of these line strengths can be very sensitive to plasma densities and/or UV fluxes (Blumenthal et al. 1972).

In actively accreting T Tauri (pre-main sequence) stars, HETGS observations can be used to distinguish between coronal (low density) and accretion shock (high density) X-ray emitting plasma and, in the latter case, be used to estimate accretion rate. Kastner et al. (2002) measured the ratios of He-like lines of O VII and Ne IX in the actively accreting T Tauri star TW Hya which indicated a plasma density of about $10^{12.75}$ cm⁻³ which is consistent with accretion. This region is shown in Fig. 2 (left). Subsequent deeper observations of TW Hya with HETGS by Brickhouse et al. (2010) were able to detect the density-suppressed f-line in O VII and Mg XI; they found that simple theoretical expectations of temperature-density profiles in accretion shocks were not satisfied.

The f/i ratio is also important to determinations of coronal structure in late-type stars. Testa et al. (2004) surveyed the diagnostic in a sample of stars, finding a clear upper limit to coronal densities, based on the fact that Si XIII was always at its low-density limit ($< 10^{13}$ cm⁻³), that hotter plasma is denser (10^{12} cm⁻³ for Mg XII and 10^{10} cm⁻³ for O VII), and that more active stars (higher X-ray luminosity)

have modestly higher densities.

Even higher plasma densities can occur in the accretion onto highly magnetic white dwarfs from binary companions (the “intermediate polars” class). Mauche et al. (2001, 2003) used density sensitive lines of Fe XVII and XXII to measure densities of 10^{14} cm⁻³ or greater in EX Hya (Fig. 2, right).

Doppler Line Emission in the Ultra-Compact Binary 4U1626-67

The accretion powered pulsar 4U 1626-67 is a rare example of a strongly magnetized ($\approx 10^{12}$ G) neutron star in a low-mass X-ray binary (LMXB) in contrast to more common weakly magnetized ($\approx 10^8$ G) cousins. Its ultra-compact nature implies a hydrogen-deficient companion, likely a C-O or O-Ne white dwarf with accretion material rich in C, O and Ne. Strong line complexes at Ne and O detected with ASCA (Angelini et al. 1995) were resolved with the *Chandra* HETGS into Doppler-broadened line complexes (Schulz et al. 2001) with blue- and red-shifted components separated by over 4000 km s⁻¹. In 2008 the pulsar experienced a torque reversal and went into a spin-up. The X-ray flux jumped by several factors and the Doppler line complexes (shown in Fig. 3) could now be identified as broad disklines originating at the boundary of the pulsars magnetosphere. Detailed plasma model fits to the HETGS spectrum also revealed that the X-ray line emission is a result of collisional ionization at the boundary of the magnetosphere and likely a result of coronal type magnetic reconnection processes (Schulz et al. 2019).

Structure and Conditions of the SS 433 Jets

The Galactic X-ray binary SS 433 features highly relativistic red- and blue-shifted emission lines whose Doppler shifts vary sinusoidally. The so-called kinematic model (e.g. Margon & Anderson, 1989) gives the time dependence of the oppositely-directed jets, whose average bulk velocity is about 0.26c, and which precess with a 162 day period. The X-ray spectra are best described by thermal emission from an expanding gas, cooling from a temperature over 10^8 K. HETGS spectra (Fig. 4) have been used to show that the gas doesn't change speed as it cools and the opening angle of the flow is about 1.2 deg, probably set by the temperature at the base (Marshall et al. 2002). The HETGS spectra also show that the gas is overabundant in metals by 2 times over solar, with Ni being overabundant by a factor of 15, perhaps an indication that the compact object resulted from an unusual supernova. Also, HETGS data taken during an eclipse by the companion were used to constrain the length of the jets to less than 2×10^{12} cm and the density at the base to 10^{10-13} cm⁻³ (Marshall et al. 2013).

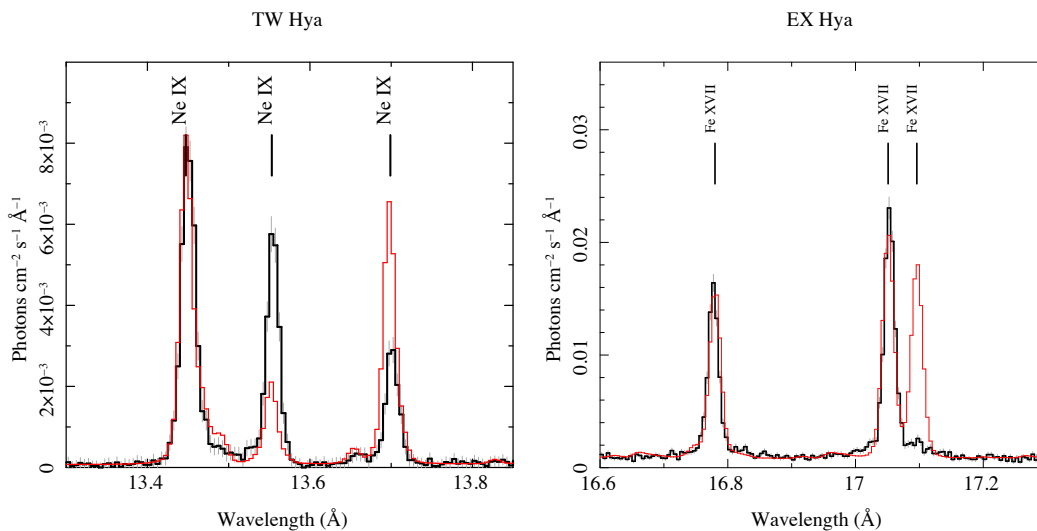


Figure 2: Left: The Ne IX *f* (13.7 Å) and *i* (13.55 Å) lines are sensitive to density; their sum, relative to the 13.44 Å *r* line is sensitive to temperature. The black curve shows the 500 ks MEG spectrum of the pre-main-sequence star TW Hya in this region. The red curve is a model spectrum at the low density limit (with the appropriate temperature of about 2 MK). The observed ratio requires a density of about $3.0 \times 10^{12} \text{ cm}^{-3}$. Right: The Fe XVII 17.10 Å line, relative to Fe XVII 16.78 Å, is sensitive to density for densities above 10^{13} cm^{-3} . The black curve shows the 500 ks MEG spectrum of the accreting magnetic white dwarf binary system (an "intermediate polar") EX Hya in this region. The red curve is a model spectrum at the low density limit. The observed ratio requires a density in excess of 10^{14} cm^{-3} , or photoexcitation by a radiation field in excess of 55 kK assuming blackbody emission.

Winds in the Black Hole Binary GRS 1915+105

The stellar mass black hole GRS 1915+105 is unique for its high luminosity, its bright, variable, and superluminal radio jets, the 27-year duration of its current outburst, and its impressive array of erratic, high-amplitude X-ray variability. In addition, the black hole is a strong source of narrow absorption lines from an accretion disk wind, whose properties vary with the X-ray state (e.g. Lee et al. 2002; Neilsen & Lee, 2009; Miller et al. 2015, 2016). The appearance of an ionized wind in the presence of strong variability in the radiation field provides an unrivaled opportunity to track the time-dependent evolution of a black hole outflow. Indeed, time-resolved spectroscopy with the HETGS reveals complex changes in the ionization state of the wind that are measurable on timescales as short as 5 seconds. Combined with measurements of the broadband spectrum, these changes make it possible to infer variations in the mass loss rate of the wind itself, which may be as large as 25 times the accretion rate (Neilsen et al. 2011). In Fig. 5 (left), we show an example of data taken when the source was exhibiting 30-minute oscillations, called the β state. HETGS spectra from high- and low-flux intervals indicate an absorber whose column density changes significantly over this cycle but whose ionization parameter is nearly constant; this is consistent with a wind launching mechanism that only operates at high flux (Neilsen et al. 2012b).

primary shock radius of $\sim 20''$ (6.4 pc) and an estimated age of 1000 yr. Its moderate extent and the dominance of X-ray line emission makes it an excellent target for HETGS observations. The dispersed spectrum is analogous to a spectroheliogram, showing a series of monochromatic images of the source in the light of individual spectral lines. Fig. 6 shows the dispersed image of the reverse-shocked ejecta in E0102-72 in the light of O VII (He-like resonance, Left) and O VIII (H-like, Right) lines. It is clear that the more ionized H-like oxygen lies at larger radii (by $\sim 1''$ – $2''$). Because the plasma is still ionizing slowly at these low densities, the images trace the progression of the reverse shock, which proceeds from larger to smaller radii (in the frame of the expanding remnant) as the ejecta are slowed by the surrounding medium. This trend of ionization age vs. radius is confirmed and refined by study of multiple ionization states of different elements (Flanagan et al. 2004). The authors estimate that $\approx 6 M_{\odot}$ of Oxygen are emerging from this core-collapse explosion of a massive star. Doppler velocities of up to $\pm 1000 \text{ km s}^{-1}$, which appear as small distortions of the image in the dispersion direction, suggest the remnant forms a non-uniform spherical shell inclined to the line of sight.

Photoexcitation of Gas Outflowing from the Nucleus of NGC 1068

The HETGS spectrum of NGC 1068 (Fig. 7) is dominated by strong emission lines that are well resolved spectral-

Miller et al. (2015, 2016) pushed the power of the HETGS by studying the third order HEG spectrum of GRS 1915+105. This gives three times the normal first order spectral resolution (or $\approx 12 \text{ eV}$ at 7 keV), albeit with only a small fraction of the effective area. This high resolution reveals the doublet structure of the Fe xxvi H-like Ly- α absorption line and separates the resonance and inter-combination lines of He-like Fe xxv (see Fig. 5, Right). The authors find four wind components with velocities up to 0.03 c, and they deduce launching radii of $r \approx 10^{2-4} \text{ GM}/c^2$.

Imaging the Reverse Shock in SNR E0102-72

E0102-72 is a well-studied member of the oxygen rich class of supernova remnants. It is located in the SMC, has a primary

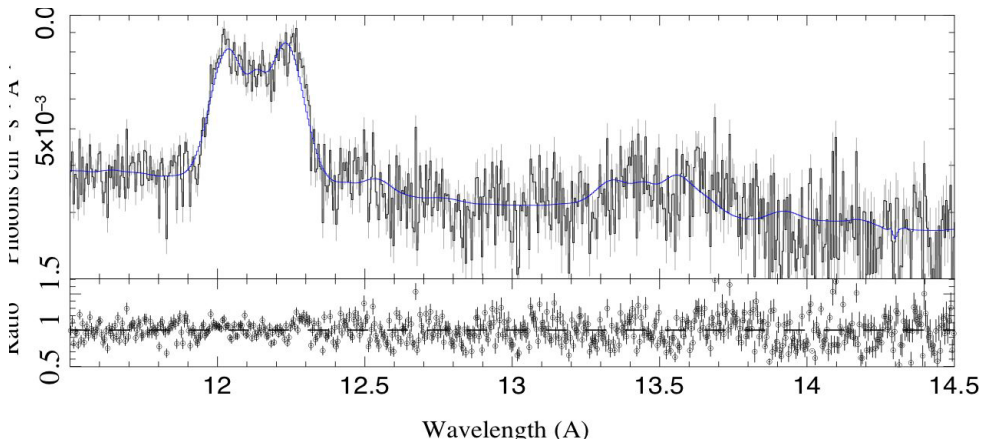


Figure 3: Spectral fit of the Ne x (12 Å) and ix (13.5 Å) regions of the 2010 HETG observation using a collisional ionized plasma model and diskline functions of 4U1626-67.

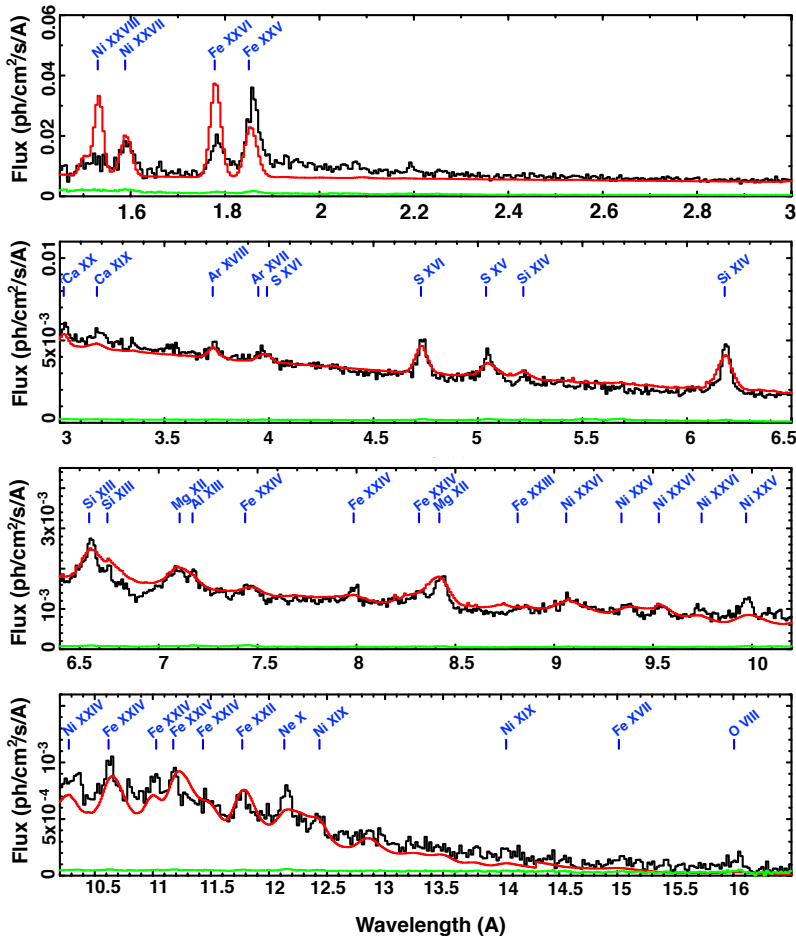


Figure 4: X-ray spectrum of SS 433 from HEG (top panel only) and HEG+MEG after correcting for the Doppler shift of the blueshifted jet (Marshall et al. 2013). Green line: Statistical uncertainties in the flux measurements. Red line: Four temperature plasma model providing an adequate fit to the spectrum. Residuals near 2 Å are primarily due to the redshifted jet's continuum, which is somewhat weaker than those of the blueshifted jet. Lines are identified where there are features in the spectrum accounted for by the model.

ly. The high signal spectrum (450 ks) was analyzed in detail by Kallman et al. (2014), building on previous work by Young et al. (2001), Kinkhabwala et al. (2002), and Ogle et al. (2003). Over 80 lines were identified from a wide range of ionization states resulting from photoexcitation by nuclear X-ray emission. Outflows of 450 km s⁻¹ were found and lines are also broadened by > 1200 km s⁻¹. The best fitting model consisted of three photoionized emitters ranging in log ξ from 1 to 3 (where ξ is the ionization parameter) with a filling factor of only a few percent. Most of the emitting gas is actually found beyond 100 pc from the core and has a substantial mass outflow rate of $\sim 0.3 M_{\odot} \text{ yr}^{-1}$, ~ 10 times greater than the nominal accretion rate.

Still Going Strong at 40

The current state of the HETGS is strong. The spectral resolution and the line-spread function remain unchanged since launch. However, the build-up of contamination on the ACIS-S optical blocking filter has degraded the effective area below 2 keV (see Chapters 6 and 8 of the *Chandra* Proposers Observatory Guide (POG): (<http://cxc.harvard.edu/proposer/POG/>). For example, the effective area at the O VIII Ly- α line at 0.654 keV has decreased to $\sim 6\%$ of its value at launch. The good news is that the band above 2 keV is only modestly affected (effective areas of $\sim 70\%$ the launch value at 1 keV and $\sim 92\%$ at 2.5 keV). So, having reached middle age, the HETGS at 40 continues to be a unique and powerful probe of astrophysical processes in the cosmos.

Bibliography

Angelini, L., White, Cranmer, S. R., N. E., Nagase, F., et al. 1995, *ApJ*, 449, L41
 Dupree, A. K., Luna, G. J. M., & Wolk, S. 2010, *ApJ*, 710, 1835
 Blumenthal, G. R., Drake, G. W. F., & Tucker, W. H. 1972, *ApJ*, 172, 205
 Canizares, C. R., Davis, J. E., Dewey, D., et al. 2005, *PASP*, 117, 1144
 Brickhouse, N. S., Cassinelli, J. P., Miller,

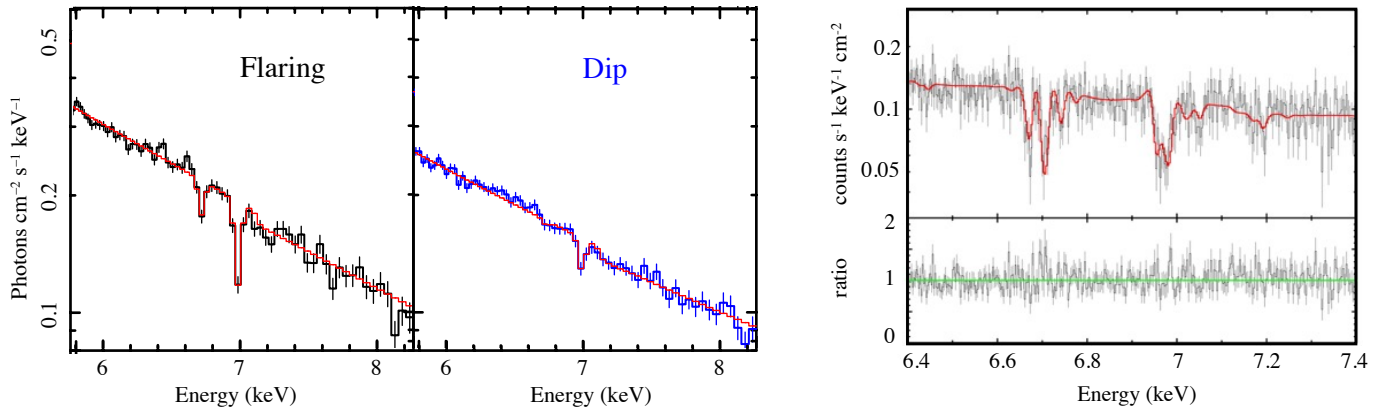


Figure 5: Left: The *Chandra* HETGS spectra and residuals for the flaring and dip intervals of the state of GRS 1915+105. We detect strong absorption lines from Fe xxvi during both time periods, and Fe xxv during the X-ray flaring (Neilsen et al. 2012b) Right: Third-order HETG spectrum of GRS 1915+105 with best-fit model. Four photoionization zones with paired absorption and re-emission are required. The He-like Fe xxv line is resolved into *i* and *r* components (rest-frame energy: 6.70 keV). Instances of H-like Fe xxvi absorption lines close to the rest-frame value of 6.970 keV and blueshifted up to 7.05 and 7.2 keV are apparent. The Fe xxvi line shape is a doublet owing to the expected spin-orbit splitting in the H-like atom (Miller et al. 2016).

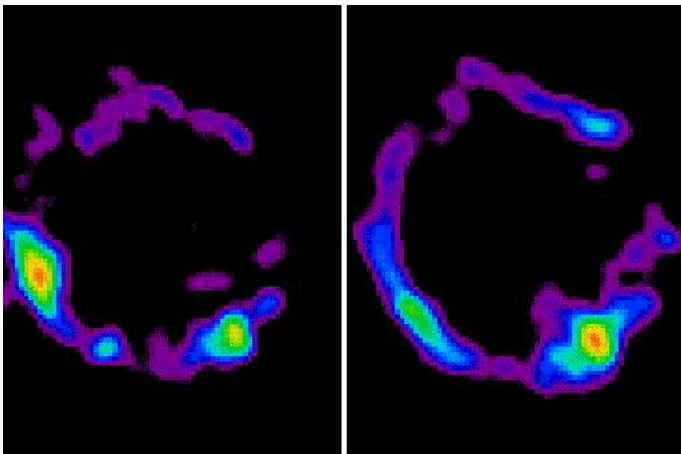


Figure 6: The HETGS dispersed image of E0102-72 in the light of O VII (He-like resonance, Left) and O VIII (H-like Ly- α , Right) lines. The images trace the progression of the reverse shock, which proceeds from larger to smaller radii (in the frame of the expanding remnant).

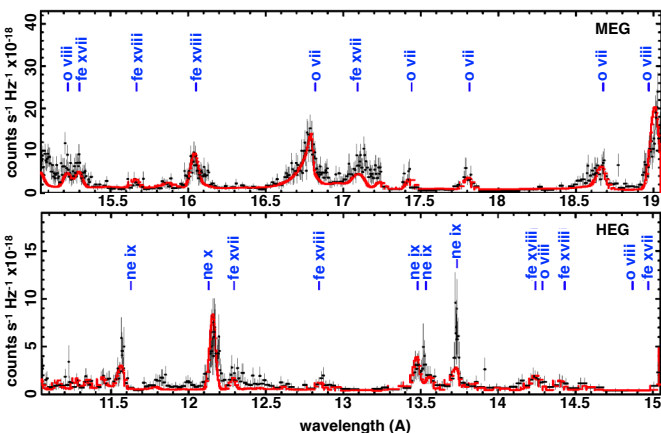


Figure 7: A portion of the HETGS spectrum of NGC 1068 obtained with MEG (top) and HEG (bottom). The best-fit model, consisting of three photoionization components, is shown in red with identified lines indicated in blue. Lines are blue-shifted by 450 km s⁻¹ and Doppler-broadened by 1500 km s⁻¹; in addition, the width of the O VII radiative recombination continuum feature (at 16.8 Å) provides an estimate of the gas temperature, which is less than 105 K.

N. A., Waldron, W. L., MacFarlane, Fournier, K. B. 2003, *ApJL*, 588, L101
 J. J., & Cohen, D. H. 2001, *ApJL*, 554, L55
 Flanagan, K. A., Canizares, C. R., Dewey, D., et al. 2004, *ApJ*, 605, 230
 Gagné, M., Oksala, M. E., Cohen, D. H., et al. 2005, *ApJ*, 628, 986
 Kallman, T., Evans, D. A., Marshall, H., et al. 2014, *ApJ*, 780, 121
 Kastner, J. H., Huenemoerder, D. P., Schulz, N. S., Canizares, C. R., & Weintraub, D. A. 2002, *ApJ*, 567, 434
 Kinkhabwala, A., Sako, M., Behar, E., et al. 2002, *ApJ*, 575, 732
 Lee, J. C., Reynolds, C. S., Remillard, R., et al. 2002, *ApJ*, 567, 1102
 Margon, B., & Anderson, S. F. 1989, *ApJ*, 347, 448
 Marshall, H. L., Canizares, C. R., & Schulz, N. S. 2002, *ApJ*, 564, 941
 Marshall, H. L., Canizares, C. R., Hillwig, T., Mioduszewski, A., Rupen, M., Schulz, N. S., Nowak, M., & Heinz, S. 2013, *ApJ*, 775, 75
 Mauche, C. W., Liedahl, D. A., & Fournier, K. B. 2001, *ApJ*, 560, 992
 Mauche, C. W., Liedahl, D. A., & Fournier, K. B. 2003, *ApJL*, 588, L101
 Miller, J. M., Fabian, A. C., Kaastra, J., et al. 2015, *ApJ*, 814, 87
 Miller, J. M., Raymond, J., Fabian, A. C., et al. 2016, *ApJL*, 821, L9
 Neilsen, J., & Lee, J. C. 2009, *Nature*, 458, 481
 Neilsen, J., Remillard, R. A., & Lee, J. C. 2011, *ApJ*, 737, 69
 Neilsen, J., Remillard, R. A., & Lee, J. C. 2012, *ApJ*, 750, 71
 Neilsen, J., Petschek, A. J., & Lee, J. C. 2012, *MNRAS*, 421, 502
 Ogle, P. M., Brookings, T., Canizares, C. R., Lee, J. C., & Marshall, H. L. 2003, *A&AP*, 402, 849
 Schulz, N. S., Chakrabarty, D., Bibi Marshall, H. L., et al. 2001, *ApJ*, 563, 941
 Schulz, N. S., Canizares, C., Huenemoerder, D., & Tibbets, K. 2003, *ApJ*, 595, 365
 Schulz, N. S., Chakrabarty, D., & Marshall, H. L. 2019, in prep
 Testa, P., Drake, J. J., & Peres, G. 2004, *ApJ*, 617, 508
 Young, A. J., Wilson, A. S., & Shopbell, P. L. 2001, *ApJ*, 556, 6